Spatially Resolved Spectroscopic Extreme Ultraviolet Reflectometry for Laboratory Applications

Maksym Tryus, Stefan Herbert, Daniel Wilson, Lukas Bahrenberg, Serhiy Danylyuk, Larissa Juschkin

Article

Journal of
Nanoscience and Nanotechnology
Vol. 19, 562–567, 2019
www.aspbs.com/jnn

Spatially Resolved Spectroscopic Extreme Ultraviolet Reflectometry for Laboratory Applications

Maksym Tryus[1, 4, *], Stefan Herbert[2, 4], Daniel Wilson[1, 3, 4], Lukas Bahrenberg[2, 4], Serhiy Danylyuk[2, 4], and Larissa Juschkin[1, 3, 4]

[1] Chair for Experimental Physics of Extreme Ultraviolet, RWTH Aachen University, Steinbachstr. 15, 52074 Aachen, Germany
[2] Chair for Technology of Optical Systems, RWTH Aachen University and JARA-FIT, Steinbachstr. 15, 52074 Aachen, Germany
[3] Peter Grünberg Institut, Forschungszentrum Jülich GmbH, 52425 Jülich, Germany
[4] JARA-FIT – Jülich Aachen Research Alliance for Fundamentals of Future Information Technology, Forschungszentrum Jülich GmbH, 52425 Jülich, Germany

Spatially resolved extreme ultraviolet reflectometry is presented in application to a local characterization of thin non-uniform contamination layers. Sample reflectivity mapping is performed, demonstrating high chemical sensitivity of the technique. Amorphous Al_2O_3 and carbon are determined as the contaminants of the studied silicon wafer. The results correlate with those obtained by energy-filtering photoemission electron microscopy. A laboratory tool is developed that is capable of multi-angle (2°–15°) and spectrally broadband (9.5–17 nm) extreme ultraviolet reflectometry at grazing incidence combined with a reduced sample illumination spot size, enabling spatially resolved metrology. A minimum EUV spot size of 25×30 μm in the sample plane is achieved experimentally.

Keywords: Extreme Ultraviolet, Reflectometry, Contamination, Spatial Resolution.

1. INTRODUCTION

Over the past decades, extreme ultraviolet (EUV) reflectometry has become a well-established non-destructive technique for the characterization of thin films and layered structures.[1, 2] At first driven by the need for diagnostic tools in the field of EUV lithography, the technique is not restricted anymore to only at-wavelength characterization of EUV mirrors and mask-blanks—spectrally broadband reflectivity measurements allow to investigate almost arbitrary structures.[3]

EUV reflectometry constantly continues to develop as the demand for thin film diagnostics keeps increasing. It offers high chemical sensitivity due to the strong interaction of EUV radiation with matter, being able to resolve ultra-thin layers with sub-nanometer thickness variations.[4] A coupling of the method with X-ray reflectometry is especially prominent for the characterization of complex layered systems, benefiting from the strong sides of both techniques.[5] The short wavelength of EUV is advantageous for achieving a spatial resolution higher than visible light can offer, and the accessible range of grazing incidence angles is larger in comparison with X-ray reflectometry.

EUV reflectometry setups, conventionally deployed at synchrotron facilities[6–9] provide the essential metrology for a wide variety of applications,[10] but due to the limited user access with a rather long waiting list they are not suitable for regular industrial applications. Therefore, several off-synchrotron laboratory tools for express on-site metrology were developed.[11–18] Based on compact laser- and discharge-produced plasma EUV radiation sources, they can cover virtually the same range of applications as synchrotron-based systems, enabling laboratory research and industrial metrology.

The design trend of EUV reflectometers moves towards a combination of angle-resolved and spectrally broadband measurements, which allows to collect more information about the sample using a single tool. Still, many reflectometers use either a single-wavelength[11–13] or a tunable monochromatic[14, 15] approach, which is more time consuming than the spectrograph-based one with a full spectrum acquisition,[3] employed in our setup.

Most available lab-based EUV reflectometers do not feature high spatial resolution. Their EUV spot sizes on

*Author to whom correspondence should be addressed.

 1533-4880/2019/19/562/006 doi:10.1166/jnn.2019.16470

the sample exceed 0.5 mm at normal incidence in at least one dimension.[11–16] Currently, among the laboratory tools, the smallest reported EUV spot size (30×75 μm) is achieved[19] using a Kirkpatrick-Baez focusing optics. This setup, being one of the most advanced, takes advantage of the polychromatic approach, yet it has a moveable spectrograph shoulder without a dedicated reference detector, which slows down the data acquisition process.

2. EXPERIMENTAL DETAILS

Spatially resolved EUV reflectometry allows to study non-uniform samples, characterize small sample features and/or perform reflectivity mapping of specific areas of interest. This can be done on the off-synchrotron laboratory basis with our table-top EUV reflectometer, called the Polychromatic Angle-resolving Non-destructive Tool for High-speed Extreme-ultraviolet Reflectometry (PANTHER). It is based on a compact gas discharge-produced plasma (DPP) source from RI Research Instruments GmbH.[20] Depending on the source working gas, different spectral ranges are accessible. The utilized krypton/xenon mixture,[4] for instance, provides broadband EUV emission within 9.5–17 nm. A general view and the operation scheme of the tool can be found in Figure 1.

Every pulse of EUV radiation from the source produces two simultaneously measured spectra—before and after the reflection by the sample, at a certain angle of incidence. These two spectra are formed by means of two spherical diffraction gratings (both are identical gold-coated flat-field holographic gratings, effective in grazing incidence). The first diffraction grating also serves a purpose of the sample illumination with its 0th order. The 1st diffraction order of the first grating is detected by a custom-built CCD detector that features a Hamamatsu S9840 sensor, while a state of the art camera (Andor DX 440-BN) is used along with the second grating.

Angle-resolved reflectance measurements without a rotating spectrograph shoulder are enabled by mounting a deflection mirror on one rotational stage with the sample. This mirror is moved parallel to the sample keeping the reflected beam position constant at the second grating within the entire range of accessible grazing incidence angles (2°–15°). The sample itself is mounted on a separate linear positioner that allows its scanning across the EUV beam with a minimum step size of 50 nm.

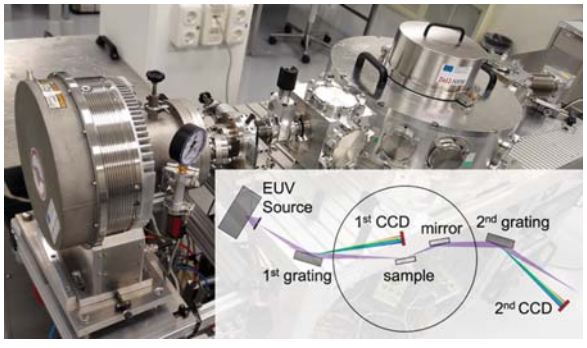

Figure 1. Photo of the EUV reflectometer. The inset shows the operation scheme of the tool (horizontal plane).

The absolute reflectivity of an unknown sample at a given angle of incidence is obtained from two pairs of spectra. One pair comes from the two CCD detectors in a measurement done with the sample of interest and the other pair corresponds to a calibration measurement with a reference sample of known reflectance (usually carbon). The resulting reflectivity is calculated by the following equation:

$$R(\theta, \lambda) = \frac{I_2^{\text{sam}}}{I_1^{\text{sam}}} \frac{I_1^{\text{ref}}}{I_2^{\text{ref}}} R^{\text{ref}}$$

The reflectivity calculation procedure can be executed during the measurement in real time, and the displayed reflectivity curve is updated with every exposition, demonstrating the improving noise statistics.

3. RESULTS AND DISCUSSION

3.1. Study of Sample Contamination Using Spatially Resolved EUV Reflectometry

During the development of an EUV source by our industrial partner, a study of the contamination of EUV collection optics due its proximity to the EUV source has been performed. In the course of the study, a test sample (silicon wafer) was placed in the vicinity of the source and exposed to the local environment during the source operation, which created two separate contamination fields (Fig. 2(a)). The details of the experimental arrangement as well as the partner's name cannot be disclosed due to the confidentiality agreement.

In order to analyze the resulting contamination, the absolute reflectivity of the sample was measured with the PANTHER at a fixed grazing incidence angle of 8° in spatially resolving mode by scanning the sample horizontally across the EUV beam with a stepwise movement. The grazing angle of incidence was chosen to provide the illumination spot small enough while maintaining a sufficient reflectivity level. The size of the beam footprint at 8° was about 400 μm in the scanning direction, which is smaller than the separation of the two regions. This allowed to obtain a clear contrast between the sample areas. The reflectivity spectra measured in 17 positions were combined in a reflectivity map, showing the transition between the two separate contamination regions (Fig. 2(b)).

Two reflectivity curves representing two distinct sample areas ($X = 0$ and 3 mm) were fitted to a model with the software package IMD[21] in order to characterize their chemical composition and layer structure (Fig. 3). The central part of the silicon wafer ($X = 0$ mm) shows the presence of a silicon oxide layer (4 nm), perhaps formed naturally before exposition. Adding to the model a non-uniform rough layer of carbon (2.5 nm) on top allowed

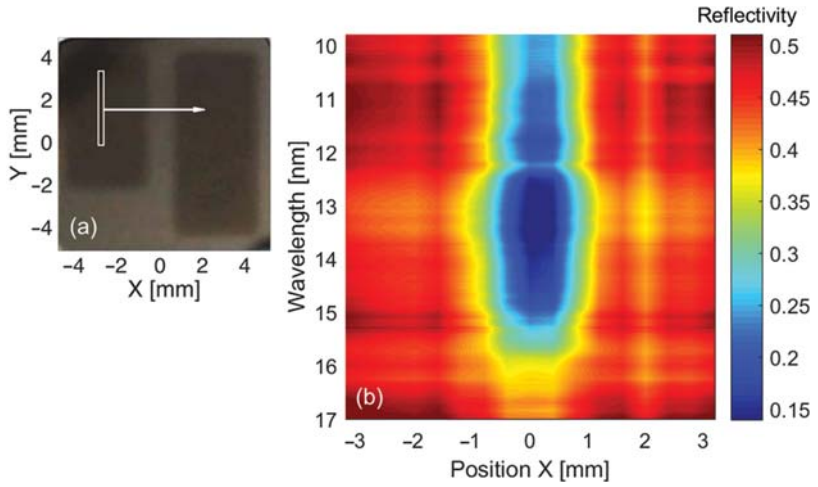

Figure 2. (a) Studied Si sample with two contamination regions. The EUV spot footprint and the scan direction are marked. (b) Resulting spectral reflectivity map of the sample.

to reach the convergence. Carbon is widely reported as a usual contaminant of EUV optics,[22] assigned to hydrocarbon dissociation under EUV irradiation.[23]

Reflectivity, measured in the neighboring dark area ($X = 3$ mm) differs from the latter drastically. Apart from the noticeable reflectivity level increase, a few other dissimilarities can be pointed out. Firstly, the $L_{II,III}$ absorption edge features of silicon, clearly visible in the first area below 12.4 nm, are vastly diminished, leaving only weakly traceable remnants. It indicates that the newly formed contamination layer has a thickness comparable to the penetration depth of EUV radiation at the given incidence angle. Furthermore, two new minima appear at 15.7 and 16.2 nm, giving a key to the determination of composition of the contamination layer. They are interpreted as a near-edge feature of the deposited material. The double-minima feature itself looks like a characteristic near-edge "fingerprint" of an amorphous oxide—a similar reflectivity shape, but near the Si $L_{II,III}$ edge can be spotted in studies of silicon oxides.[24] In our experimental results, its observed position below 17 nm, close to Al $L_{II,III}$ edge, indicates the presence of an amorphous aluminum oxide, which is supported by other studies.[25]

Constructing a layer model that resembles a contaminated sample can be a challenging task because of the complexity and non-uniformity of real contamination layers. Furthermore, when fitting their reflectivity, one can rely solely on the available experimentally obtained refractive indices, which represent a certain chemical composition and structure. It also limits the fit flexibility in the near-edge regions. For the amorphous aluminum oxide layer, the set of optical constants tabulated by Hagemann[26] was used.

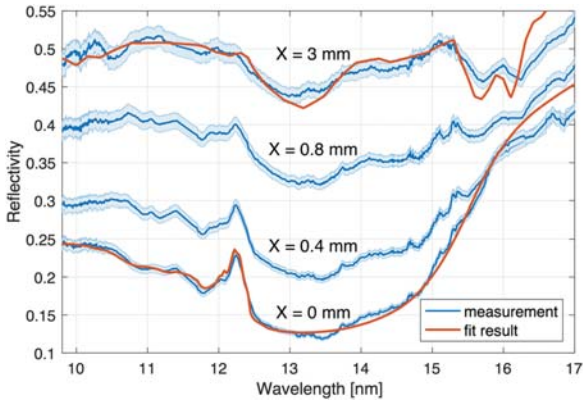

Figure 3. Reflectivity spectra (blue) and the fit results (red) at different X positions on the sample, from top to bottom: 3 mm, 0.8 mm, 0.4 mm, 0 mm.

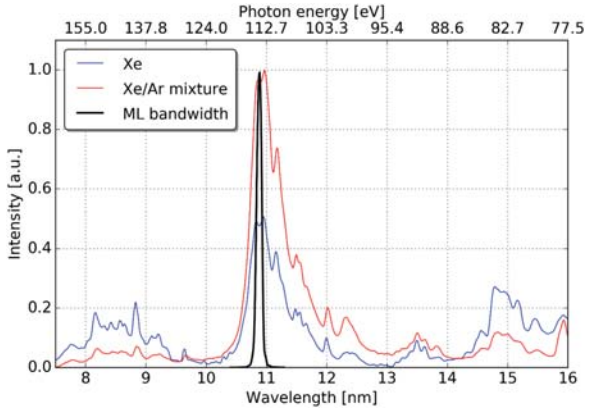

Figure 4. EUV emission spectra of pure Xe (blue) and Xe/Ar mixture (red) utilized for the photoemission electron microscopy. Bandwidth of the combination of two ML-mirrors is shown in black.

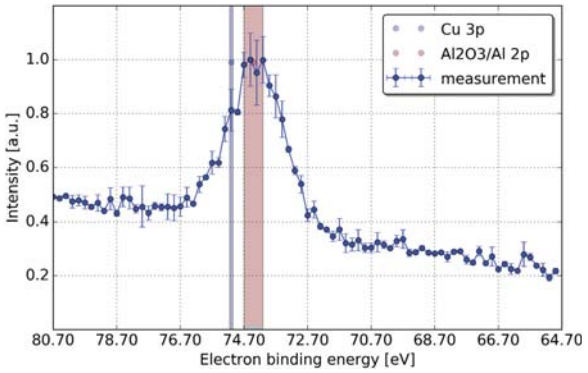

Figure 5. Section of the photoelectron spectrum measured at 113.7 eV photon energy. Electron binding energies of the materials that fit within the peak are highlighted.

Besides aluminum, some other metals were tested as possible contaminants, but could not be fitted to the observed spectral reflectivity dependence. On the other hand, carbon is likely to be present in the contamination, improving the fit convergence. As carbon could not be incorporated into the Al_2O_3 layer directly, it had to be represented by an effective layer on top. The best fit result, shown in Figure 3 (top curve), has 0.7 nm of carbon and 10 nm of amorphous Al_2O_3 topping the oxidized silicon wafer. The thickness of the SiO_2 layer was assumed equal to the previous result (4 nm).

3.2. Cross-Correlation with Photoemission Electron Microscopy

To verify the findings by means of another element-sensitive technique, further measurements were performed using a combination of a state-of-the-art energy-filtering photoemission electron microscope (EF-PEEM) with a gas discharge EUV source.[27] Instead of oxygen as the source fuel, a xenon/argon mixture[28] was used to achieve a higher photon energy. Compared to pure xenon, this mixture exhibits twice as many photons around 11 nm. Additionally, wavelength $\lambda = 10.9$ nm (photon energy $E = 113.7$ eV) was filtered by two narrow-bandwidth multilayer (ML) mirrors (Fig. 4). The spectral bandwidth $\Delta\lambda$ of the combination was 0.1 nm (FWHM), which corresponded to $\Delta E = 1$ eV.

The measured photoelectron spectrum of the contaminated sample (dark area in Fig. 2) contains one prominent peak at 74.5 eV, which can be seen in Figure 5. In contrast to the measurements reported in Ref. [27], the energy resolution here is limited by the bandwidth of the ML-mirrors, resulting in the peak FWHM of 1.84 eV. Two materials fit to this range simultaneously—oxidized aluminum and copper. From the EF-PEEM results only, one cannot clearly distinguish between them. The EUV reflectivity measurements done with the PANTHER, on the other hand, clearly show the presence of aluminum oxide, ruling out the copper content, which also fits to the sample history. The carbon contamination, suggested by the reflectivity analysis, could not be tested with the EF-PEEM, as the used photon energy of 113.7 eV was lower than the electron binding energy of the carbon K-shell.

3.3. Spatial Resolution of the PANTHER

For certain demanding applications, such as investigating samples with local features on the submillimeter scale or patterns that benefit from reflectivity mapping, the size of the illumination footprint on the sample is crucial. In this regard, spatially resolving capabilities of the PANTHER and its potential for improvement shall be discussed.

The originally developed PANTHER setup[4] featured a slit-like sample illumination with a footprint of

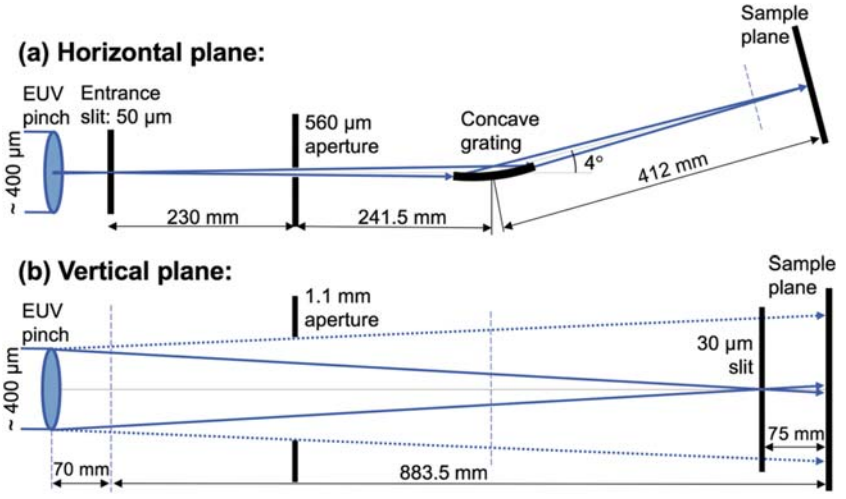

Figure 6. Sample illumination scheme in two principal planes of the reflectometer, with a 30 μm slit in front of the sample plane. Beam path without this slit is shown with the dotted line.

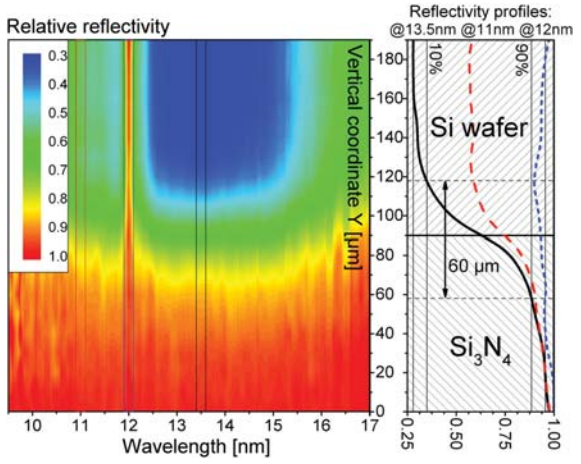

Figure 7. Relative reflectivity scan at 8° grazing incidence across an abrupt horizontal Si/Si_3N_4 field border with the vertical sample movement (left). Reflectivity profiles at 11, 12 and 13.5 nm; knife-edge resolution test at 13.5 nm (right).

55 μm/sin$\theta \times 3.5$ mm, where the horizontal dimension of the footprint depends on the grazing incidence angle θ on the sample. The sample illumination scheme of the reflectometer can be found in Figure 6. For the utilized Kr/Xe gas mixture, the diameter of the EUV-emitting plasma pinch is roughly about 400 μm (FWHM). A vertical entrance slit of 50 μm width acts as an effective light source for the spherical diffraction grating, which images the entrance slit into the sample plane. The grating is imaging only in the horizontal (grazing incidence) plane, while the beam in the vertical plane is diverging, only slightly affected by the spherical grating curvature (dotted line in Fig. 6(b)). The intermediate aperture of 560×1100 μm limits the beam between the entrance slit and the grating, blocking undesired stray light.

Without major alterations to the illumination scheme, it is possible to gain spatial resolution only at the cost of lower photon flux. When having a slit-like beam footprint in the sample plane, a straightforward approach would be to reduce its height. For this purpose, a 30 μm slit was installed in front of the sample plane horizontally (Fig. 6(b)). Acting as a pinhole camera, it produces a demagnified image of the EUV-emitting plasma pinch in the vertical sample plane, not affecting the horizontal beam path.

In order to characterize the achieved resolving capabilities of the tool, a knife-edge resolution test was performed. For this particular task, a partially nitrided silicon wafer with a straight sharply etched field border was taken. One field contained a 50-nm thick layer of Si_3N_4 on top of the wafer, whereas the nitride was etched out completely from the second field, leaving the bare Si substrate with only a few nanometers of naturally grown oxide on top. The sample was scanned by a vertical movement across the field border at 8° grazing incidence angle, measuring relative reflectivity (the nitrided field was set as the reference). Assuming that the reflectivity within each field at a certain wavelength is uniform, and the field border is sharp, the resolution is then defined as the distance between positions with 10% and 90% relative reflectivity levels. The results are shown in Figure 7. The highest reflectivity contrast was observed in the region below the Si $L_{II,III}$ edge (wavelengths >12.4 nm), where nitrogen in the compound has the most significant impact. From the reflectivity profile at 13.5 nm, a vertical resolution of 60 μm was determined.

Two reflectivity profiles above the Si absorption edge are plotted for comparison (Fig. 7, right). The one at 11 nm shows less contrast than the one at 13.5 nm, but has de facto the same resolution. A peculiar wavelength for the given material combination was 12 nm, exhibiting almost no change in relative reflectivity due to the dominating influence of silicon. This highlights the importance of the spectrally broadband measurements.

Discussing the highest resolution possible to achieve with the current setup, three main factors should be

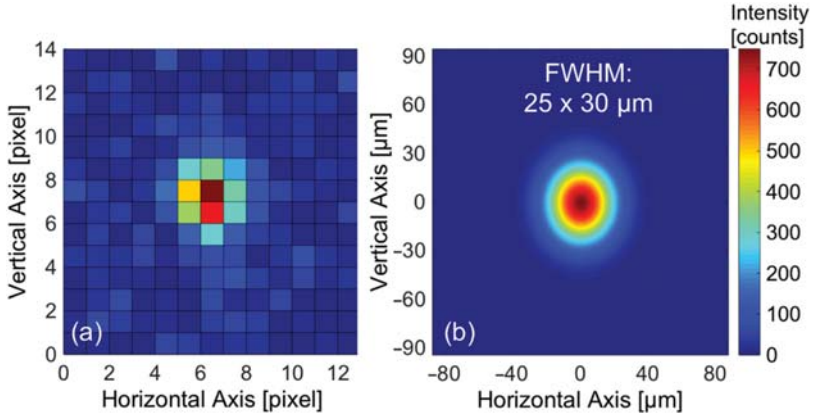

Figure 8. (a) CCD image of the illumination spot in the sample plane perpendicularly to the beam. (b) 2D Gaussian fit of the CCD image with calculated FWHM.

considered: geometry, diffraction and aberrations of the grating. Even having the first two optimized, the latter will be limiting the tool performance. The estimated minimal size of the sample illumination spot, given by the grating manufacturer, was around 20 μm at normal incidence. To test it experimentally, the entrance slit was replaced by a 10×60 μm aperture, which additionally collimated the beam in the vertical plane. A CCD camera (Andor DX440-BN) was placed directly in the sample plane perpendicularly to the beam, and a Nb filter[29] was introduced into the beam path to block the longer-wavelength light. The measured spot image and its Gaussian fit are shown in Figure 8. The determined FWHM values of the spot are 25×30 μm.

The small illumination footprint, as a matter of fact, limits the tool throughput, necessitating a compromise between the spatial resolution and the acquisition time. This trade-off can be overcome by a more power-efficient illumination focusing, which however would require a new optical design and manufacturing of the diffraction gratings.

4. CONCLUSIONS

The present contribution is focused on spatially resolved EUV reflectometry, which is particularly advantageous for studies of non-uniform samples. A silicon wafer containing a non-uniform contamination layer is characterized, demonstrating the high chemical sensitivity of the technique, agreeing with EF-PEEM results.

The developed laboratory tool is capable of multi-angle, spectrally broadband and spatially resolved EUV reflectivity measurements. A sample illumination spot size close to the minimum possible in this setup configuration was experimentally achieved. Depending on the specific research purpose, the spot size can be adjusted to ensure an optimal tool performance.

Acknowledgments: Maksym Tryus acknowledges financial support from the EU FP7 Erasmus Mundus Joint Doctorate Programme EXTATIC under framework partnership agreement FPA-2012-0033. Larissa Juschkin acknowledges financial support by the Helmholtz Association for a Helmholtz Professorship as a part of the Initiative and Networking Fund.

References and Notes

1. M. Banyay, L. Juschkin, T. Bücker, P. Loosen, A. Bayer, F. Barkusky, S. Döring, C. Peth, K. Mann, H. Blaschke, I. Balasa, and D. Ristau, *Proc. SPIE* 7361, 736113 (**2009**).
2. S. Döring, F. Hertlein, A. Bayer, and K. Mann, *Appl. Phys. A* 107, 795 (**2012**).
3. M. Banyay and L. Juschkin, *Appl. Phys. Lett.* 94, 63507 (**2009**).
4. S. Danylyuk, S. Herbert, P. Loosen, R. Lebert, A. Schäfer, J. Schubert, M. Tryus, and L. Juschkin, *Phys. Status Solidi* 12, 318 (**2015**).
5. S. N. Yakunin, I. A. Makhotkin, K. V. Nikolaev, R. W. E. van de Kruijs, M. A. Chuev, and F. Bijkerk, *Opt. Express* 22, 20076 (**2014**).
6. E. M. Gullikson, S. Mrowka, and B. B. Kaufmann, *Proc. SPIE* 4343, 363 (**2001**).
7. L. Pasquali, A. De Luisa, and S. Nannarone, *AIP Conf. Proc.* 705, 1142 (**2004**).
8. C. Laubis, A. Barboutis, M. Biel, C. Buchholz, B. Dubrau, A. Fischer, A. Hesse, J. Puls, C. Stadelhoff, V. Soltwisch, and F. Scholze, *Proc. SPIE* 8679, 867921 (**2013**).
9. C. Tarrio, S. Grantham, M. B. Squires, R. E. Vest, and T. B. Lucatorto, *J. Res. Natl. Inst. Stand. Technol.* 108, 267 (**2003**).
10. C. Laubis, F. Scholze, and G. Ulm, *Proc. SPIE* 7101, 71011U (**2008**).
11. N. Kandaka, H. Kondo, K. Sugisaki, and T. Oshino, *Proc. SPIE* 4343, 599 (**2001**).
12. K. Bergmann, O. Rosier, and C. Metzmacher, *Rev. Sci. Instrum.* 76, 43104 (**2005**).
13. A. Bayer, F. Barkusky, S. Döring, P. Großmann, and K. Mann, *X-ray Opt. Instrum.* 2010, 1 (**2010**).
14. L. van Loyen, T. Böttger, S. Schädlich, S. Braun, T. Foltyn, A. Leson, F. Scholze, and S. Müllender, *Appl. Surf. Sci.* 252, 57 (**2005**).
15. A. Miyake, T. Miyachi, M. Amemiya, and T. Hasegawa, *Proc. SPIE* 5037, 647 (**2003**).
16. R. Lebert, C. Wies, L. Juschkin, B. Jägle, M. Meisen, L. Aschke, F. Sobel, H. Seitz, F. Scholze, G. Ulm, K. Walter, W. Neff, K. Bergmann, and W. Biel, *Proc. SPIE* 5374, 808 (**2004**).
17. H. Blaschke, I. Balasa, L. Koch, K. Starke, D. Ristau, C. Wies, R. Lebert, A. Bayer, F. Barkusky, and K. Mann, *Proc. SPIE* 6922, 692228 (**2008**).
18. S. Mrowka, J. H. Underwood, E. M. Gullikson, and P. J. Batson, *Proc. SPIE* 3997, 819 (**2000**).
19. I. Balasa, H. Blaschke, and D. Ristau, *Proc. SPIE* 7969, 796928 (**2011**).
20. R. Lebert, C. Wies, B. Jaegle, L. Juschkin, U. Bieberle, M. Meisen, W. Neff, K. Bergmann, K. Walter, O. Rosier, M. C. Schuermann, and T. Missalla, *Proc. SPIE* 5374, 943 (**2004**).
21. D. L. Windt, *Comput. Phys.* 12, 360 (**1998**).
22. T. E. Madey, N. S. Faradzhev, B. V. Yakshinskiy, and N. V. Edwards, *Appl. Surf. Sci.* 253, 1691 (**2006**).
23. J. Hollenshead and L. Klebanoff, *J. Vac. Sci. Technol. B Microelectron. Nanom. Struct.* 24, 64 (**2006**).
24. E. O. Filatova, A. S. Shulakov, and V. A. Luk'yanov, *Physics of the Solid State* 40, 7 (**1998**).
25. I. Balasa, X. Neiers, M. Mende, L. Jensen, and D. Ristau, *Proc. SPIE* 9237, 92371Y (**2014**).
26. H.-J. Hagemann, W. Gudat, and C. Kunz, *DESY Report SR-74/7* (**1974**), http://dx.doi.org/10.3204/PUBDB-2018-00701.
27. C. Schmitz, D. Wilson, D. Rudolf, C. Wiemann, L. Plucinski, S. Riess, M. Schuck, H. Hardtdegen, C. M. Schneider, F. S. Tautz, and L. Juschkin, *Appl. Phys. Lett.* 108, 234101 (**2016**).
28. K. Bergmann, S. V. Danylyuk, and L. Juschkin, *J. Appl. Phys.* 106, 073309 (**2009**).
29. S. Brose, S. Danylyuk, L. Juschkin, C. Dittberner, K. Bergmann, J. Moers, G. Panaitov, S. Trellenkamp, P. Loosen, and D. Grützmacher, *Thin Solid Films* 520, 5080 (**2012**).

Received: 30 January 2017. Accepted: 26 July 2017.